

Article

# Mechanical Characteristics of Fiber-Reinforced Flexible Pipe Subjected to Axial Tensile Load

Zhenwen Sun <sup>1,\*</sup>, Weiping Huang <sup>1</sup>, Hailong Lu <sup>2</sup>, Yufeng Bu <sup>2</sup>, Yuanchao Yin <sup>3</sup> , Shichao Wang <sup>3</sup> and Yimeng Fan <sup>3</sup>

<sup>1</sup> College of Engineering, Ocean University of China, Qingdao 266100, China

<sup>2</sup> State Key Laboratory of Structural Analysis for Industrial Equipment, Department of Engineering Mechanics, Dalian University of Technology, Dalian 116024, China

<sup>3</sup> School of Ocean Science and Technology, Dalian University of Technology, Panjin 124221, China

\* Correspondence: szwmsnxz@163.com

**Abstract:** Fiber-reinforced flexible pipes are subjected to large axial tension loads in deep-water applications, which may result in the excessive deformation of the pipes. Owing to the anisotropy of the composite materials, accurately describing the tensile behavior of these pipes is difficult. Theoretical, numerical, and experimental methods are employed in this study to investigate the mechanical characteristics of a glass fiber-reinforced unbonded flexible pipe under axial tensile loads. Based on the load–strain relationship of each pipe layer, analytical equations considering the effect of anisotropy and radial deformation are first proposed to calculate the axial tensile stiffness of the pipe. A detailed numerical model is established to simulate the tensile behavior of the pipe. A prototype test is performed on a 4500 mm long sample using a tensile testing machine. The leading roles of outer tensile reinforcement layers in axial tensile capacity are illustrated by the strain energy of the pipe layers obtained by the numerical model. Subsequently, a comparison analysis of the mean fiber direction strains of the selected sections are performed between numerical and experimental results, which validates the numerical model. Additionally, the stress distributions of different pipe layers are discussed based on the results of the numerical analysis. Finally, the comparison of axial tensile stiffness results validates the accuracy of the analytical model considering radial deformation. This study proposes effective theoretical and numerical models to predict the tensile behavior of a fiber-reinforced flexible pipe, which provides useful references for the design and structural analysis of these pipes.



**Citation:** Sun, Z.; Huang, W.; Lu, H.; Bu, Y.; Yin, Y.; Wang, S.; Fan, Y. Mechanical Characteristics of Fiber-Reinforced Flexible Pipe Subjected to Axial Tensile Load. *J. Mar. Sci. Eng.* **2023**, *11*, 586. <https://doi.org/10.3390/jmse11030586>

Academic Editor: Bruno Brunone

Received: 10 February 2023

Revised: 4 March 2023

Accepted: 8 March 2023

Published: 9 March 2023



**Copyright:** © 2023 by the authors. Licensee MDPI, Basel, Switzerland. This article is an open access article distributed under the terms and conditions of the Creative Commons Attribution (CC BY) license (<https://creativecommons.org/licenses/by/4.0/>).

**Keywords:** fiber-reinforced flexible pipe; axial tensile stiffness; strain in fiber direction; analytical model; prototype test; finite element model

## 1. Introduction

Fiber-reinforced flexible pipes are a new type of offshore composite pipes manufactured by companies such as Technip [1] and DeepFlex [2] in recent years. These pipes comprise multiple reinforcement and polymer layers, similar to metal-reinforced flexible pipe [3]. However, metal-reinforced spiral belts are replaced by composite-reinforced spiral belts in fiber-reinforced flexible pipes, resulting in lower weight and better chemical and fatigue resistance.

The glass fiber-reinforced unbonded flexible pipe investigated in this study comprises nine layers, as shown in Figure 1. The liner, membrane, and outer sheath are PE (Abbreviations are all listed in notation list, see Table 1) layers formed by extrusion molding that separate the transmission medium from the external seawater. The inner hoop layer is a cylindrical structure comprising two sublayers formed by curing after cross-winding of glass fiber. The tensile and hoop reinforcement layers comprise GFRP spiral belts wound in a single direction via wet winding. Owing to the different winding angles and thicknesses, the tensile and hoop reinforcement layers contribute primarily to the axial and radial stiffness, respectively.

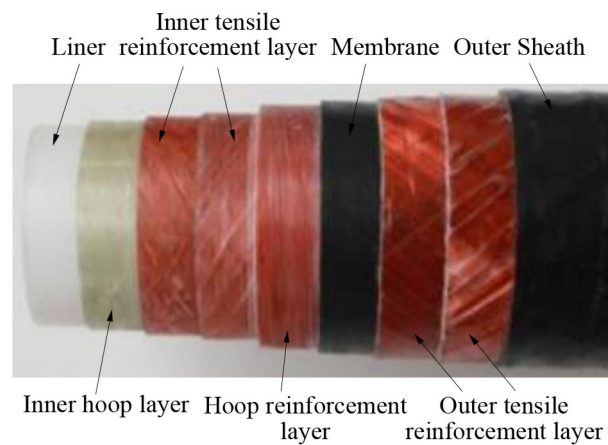


Figure 1. Sample of glass fiber-reinforced unbonded flexible pipe.

Table 1. Notation list.

Notation	Description
3D	three-dimensional
GFRP	glass fiber-reinforced plastic
PE	polyethylene
C3D8R	eight-node brick element with reduced integration
ALLIE	internal energy
ALLSE	elastic strain energy
ALLAE	artificial strain energy
ALLKE	kinetic energy
$E_1$	longitudinal tensile modulus
$E_2$	transverse tensile modulus
$G_{12}$	in-plane shear modulus
$\nu_{12}$	main Poisson ratio
$\rho$	density

The excessive deformation of pipes and the rupture of tensile armors caused by axial tensile loads are typical failure modes of flexible pipes [4]. Although the weight of fiber-reinforced flexible pipes is lower than that of typical flexible pipes, the axial tensile loads caused by the gravity of pipes in deep water are non-negligible. Therefore, the tensile stiffness and ultimate capacity of fiber-reinforced flexible pipes under axial tension must be investigated.

Some scholars have proposed analytical models to predict the tensile behavior of flexible pipes. Oliveira et al. [5] proposed a simple analytical formula based on strain and geometrical relationships to evaluate the axial stiffness of flexible pipes. Lu et al. [6] and Yue et al. [7] established theoretical models considering the radial contractions of the liner and pressure armor layers to describe the axial tensile behavior of a shallow-water flexible pipe. Tang et al. [8] proposed equations based on the tension and axial deformation relationship to calculate the tensile stiffness of umbilicals. Wang et al. [9] introduced an analytical model based on the curved beam theory to investigate the tensile mechanical behavior of flexible pipes and cables with helically wound structures.

Numerical models that considered the detailed geometries and interactions of different pipe layers were used to simulate the tensile behavior of flexible pipes. Bahtui et al. [10] performed a finite element analysis using ABAQUS/Explicit, and the results showed the hysteresis of the tensile response of a flexible pipe under a high radial pressure. Merino et al. [11] established a flexible pipe model based on beam and shell elements using ANSYS to predict the effect of end constraints and friction coefficients on the tensile response. Ren et al. [12] established a detailed finite element model based on ABAQUS/Explicit. In

consideration of the interaction between all layers, the axial tensile stiffness of an eight-layer unbonded flexible riser was predicted.

In terms of experimental research, Ramos Jr. et al. [13] conducted an axial tensile test on a flexible pipe to measure the axial and transverse strains of the outer tensile spiral belts and the axial displacement of the pipe. Lopez et al. [14] conducted a dynamic tension test on a flexible pipe and identified the rupture of tensile armors using accelerometers, inclinometers, and strain gauges. Bai et al. [15] investigated the axial tensile behavior of a steel strip-reinforced flexible pipe through a full-scale test to determine the effects of the loading rate and friction coefficient on the ultimate capacity and failure mode of the pipe. In consideration of internal pressure on the tensile response of steel strip-reinforced flexible pipes, Chen et al. [16] investigated the typical failure characteristics of the pipe via full-scale tests. A full-scale axial tensile test was conducted by Liu et al. [17] to investigate the effect of the internal friction and viscoelastic properties of polymeric layers on the axial behavior of the flexible pipe.

In consideration of the stress concentration of flexible pipes, Dong et al. [18] investigated the effects of end restraints on the stresses of the tensile armors under axial tensile loads using the finite element method. An analytical model based on strain energy and the Euler equation was also derived by Dong et al. [19] to clarify the effects of end restraints. Nassiraei and Rezadoost [20] investigated the effect of fiber-reinforced polymer layers and joint geometry on the stress concentration factors of tubular joints using finite element models and empirical formulas. Zhu et al. [21] demonstrated that ovality exerted a limited effect on the tensile stiffness of flexible pipes but resulted in stress concentrations on tensile armors. De Sousa et al. [22] and Zhu et al. [23] investigated the axial tensile response of a flexible pipe with damaged tensile armor wires; subsequently, stress concentration was observed in wires adjacent to the damaged wires.

The tensile strength of flexible pipe has also been investigated by some scholars. Goto et al. [24] proposed an equation based on the force equilibrium between the axial and circumferential directions to calculate the tensile strength of the pipe. Yim et al. [25] equated the carcass and pressure armor layer to orthotropic shells, and proposed constitutive, compatibility and force equilibrium equations for a flexible pipe; subsequently, the ultimate strength of the tensile layer was obtained using a regression analysis. Considering the plastic behavior of materials, Cornacchia et al. [26] proposed a theoretical model using the secant modulus to calculate the tensile strength of unbonded flexible pipes.

The tensile behavior of flexible pipes with composite layers has received attention in recent years. Xu et al. [27] investigated the effect of the filament winding angle, fiber volume ratio, and diameter–thickness ratio on the tensile stiffness of glass fiber-reinforced bonded flexible pipes using theoretical and finite element models. Fang et al. [28] proposed analytical and numerical models by embedding glass fibers into a matrix to simulate the mechanical behavior of a glass fiber-reinforced bonded flexible pipe under tension and internal pressure. Zhou et al. [29] investigated the tensile behavior of a flexible pipe with partial composite reinforcement layers using the finite element method, where predefined beam elements and laminated shell elements were selected for spiral belts and fiber-reinforced inner jackets, respectively. Liu et al. [30] proposed a theoretical model based on the energy method and a numerical model using ABAQUS to simulate the tensile behavior of flexible pipes with partial composite reinforcement layers.

Past research on the tensile behavior of flexible pipes has mostly focused on metal-reinforced flexible pipes, while little relevant research has been performed on fiber-reinforced unbonded flexible pipes, which are entirely composed of composite and polymer materials. The mechanical properties of composites are more complex than metal materials due to anisotropy, which leads to difficulties in research. The axial tensile behavior of a glass fiber-reinforced unbonded flexible pipe within the elastic deformation range was investigated in this study using established analytical models, while considering the anisotropy of materials and the effect of radial deformation. The classical laminate theory was used in the analytical model to obtain the engineering constants of the inner hoop layer. A

3D numerical model was established to validate the analytical model; subsequently, the distribution characteristics of the strains, stresses, and axial displacement of the pipe were obtained. Additionally, a prototype test was performed to measure the fiber-direction strain of the spiral belts in the outer tensile reinforcement layer.

## 2. Methods and Models

### 2.1. Analytical Method

For the fiber-reinforced flexible pipe used in this study, the liner, inner hoop layer, membrane, and outer sheath were modeled as cylindrical structures, whereas the inner and outer tensile reinforcement layers and hoop reinforcement layer were modeled as helical structures. The stresses and deformations of the layers under axial tensile loading are shown in Figure 2.

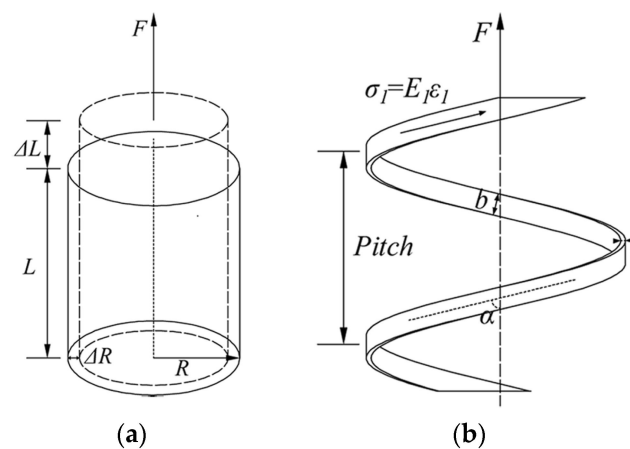


**Figure 2.** Deformation and stress of pipe layers. (a) Cylindrical layer; (b) helical layer.

The following hypotheses were proposed for the analytical model of fiber-reinforced flexible pipe subjected to axial tensile load:

1. All pipe layers are in small displacement and strain state.
2. All layers follow the plane section assumption.
3. All materials are in the linear elastic range.
4. The thickness of each layer remains constant along the axial direction of the pipe, and the spiral belts distribute uniformly along the circumferential direction.
5. All layers are subject to the same end restraints; thus, they have the same axial elongation.
6. The relative sliding between adjacent layers is not considered; thus, the effect of friction is ignored.
7. The radial separation of adjacent layers is not considered.

#### 2.1.1. Cylindrical Layers

The axial load–strain relationship of the cylindrical layer can be expressed as:

$$F_{(i)} = E_{(i)} A_{(i)} \frac{\Delta L}{L} \tag{1}$$

where  $F_{(i)}$  is the axial tensile load;  $A_{(i)}$  is the section area of the cylindrical layer;  $E_{(i)}$  is the elastic modulus of the material;  $\Delta L$  and  $L$  represent the axial elongation and initial length, respectively; and the subscript  $i$  indicates the  $i$ th layer of the pipe.

In contrast to other cylindrical layers, the inner hoop layer formed by filament winding is anisotropic; thus, the moduli differ along different directions. Using the known engineering constants of the laminas, the classical laminate theory [31] can be used to calculate the tensile elastic modulus of the inner hoop layer along the axial direction of the pipe.

For the lamina in the plane stress state, the strain–stress relationship in the principal direction of the material can be expressed by the flexibility matrix  $S$ , as follows:

$$\begin{bmatrix} \varepsilon_1 \\ \varepsilon_2 \\ \gamma_{12} \end{bmatrix} = \begin{bmatrix} S_{11} & S_{12} & 0 \\ S_{12} & S_{22} & 0 \\ 0 & 0 & S_{66} \end{bmatrix} \begin{bmatrix} \sigma_1 \\ \sigma_2 \\ \tau_{12} \end{bmatrix} = S \begin{bmatrix} \sigma_1 \\ \sigma_2 \\ \tau_{12} \end{bmatrix} \tag{2}$$

where the coefficient  $S_{ij}$  can be expressed by the fiber-direction modulus ( $E_1$ ), transverse-direction modulus ( $E_2$ ), in-plane shear modulus ( $G_{12}$ ), and main Poisson ratio ( $\nu_{12}$ ) of the lamina, as follows:

$$S_{11} = \frac{1}{E_1}, S_{12} = -\frac{\nu_{12}}{E_1}, S_{22} = \frac{1}{E_2}, S_{66} = \frac{1}{G_{12}}$$

However, the local coordinate system (i.e., 1–2) of the lamina is different from the global coordinate system (i.e., x–y) of the structure, and the angle between the 1-axis (the fiber direction of the material) and x-axis (the axis direction of the structure) is  $\theta$  (anti-clockwise implies positive direction), as shown in Figure 3. A coordinate transformation is required to obtain the off-axis engineering constants. The expansion of the transformation matrix  $T$  is expressed as:

$$T = \begin{bmatrix} \cos^2\theta & \sin^2\theta & 2\sin\theta\cos\theta \\ \sin^2\theta & \cos^2\theta & -2\sin\theta\cos\theta \\ -\sin\theta\cos\theta & \sin\theta\cos\theta & \cos^2\theta - \sin^2\theta \end{bmatrix} \tag{3}$$

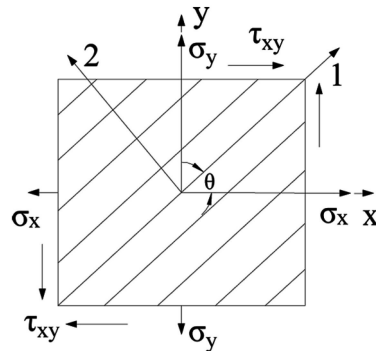


Figure 3. Local coordinate system of lamina and global coordinate system of structure.

The strain–stress relationship of the lamina in different coordinate systems can be expressed as:

$$\begin{bmatrix} \varepsilon_x \\ \varepsilon_y \\ \gamma_{xy} \end{bmatrix} = T^T \begin{bmatrix} \varepsilon_1 \\ \varepsilon_2 \\ \gamma_{12} \end{bmatrix} = T^T S \begin{bmatrix} \sigma_1 \\ \sigma_2 \\ \tau_{12} \end{bmatrix} = T^T S T \begin{bmatrix} \sigma_x \\ \sigma_y \\ \tau_{xy} \end{bmatrix} = \bar{S} \begin{bmatrix} \sigma_x \\ \sigma_y \\ \tau_{xy} \end{bmatrix} \tag{4}$$

The elastic modulus in the x-direction of the plane ( $E_x$ ) can be obtained from coefficient  $\bar{S}_{11}$  of the off-axis flexibility matrix  $\bar{S}$ .  $\bar{S}_{11}$  can be expanded as follows:

$$\bar{S}_{11} = \frac{1}{E_x} = \frac{1}{E_1} \cos^4\theta + \left( \frac{1}{G_{12}} - \frac{2\nu_{12}}{E_1} \right) \sin^2\theta \cos^2\theta + \frac{1}{E_2} \sin^4\theta \tag{5}$$

As can be inferred from Equations (3)–(5), the elastic constants in different directions of the inner hoop layer change with the fiber winding angle, which will affect the mechanical behavior of the pipe.

For the lamina in the plane stress state, the strain–stress relationship in the principal direction of the material can also be expressed by the stiffness matrix  $Q$ , as follows:

$$\begin{bmatrix} \sigma_1 \\ \sigma_2 \\ \tau_{12} \end{bmatrix} = \begin{bmatrix} Q_{11} & Q_{12} & 0 \\ Q_{12} & Q_{22} & 0 \\ 0 & 0 & Q_{66} \end{bmatrix} \begin{bmatrix} \varepsilon_1 \\ \varepsilon_2 \\ \gamma_{12} \end{bmatrix} = Q \begin{bmatrix} \varepsilon_1 \\ \varepsilon_2 \\ \gamma_{12} \end{bmatrix} \tag{6}$$

where

$$Q_{11} = \frac{S_{22}}{S_{11}S_{22} - S_{12}^2}, Q_{22} = \frac{S_{11}}{S_{11}S_{22} - S_{12}^2}, Q_{12} = \frac{-S_{22}}{S_{11}S_{22} - S_{12}^2}, Q_{66} = \frac{1}{S_{66}}$$

The off-axis stress–strain relationship of the lamina is expressed by the stiffness matrix, as follows:

$$\begin{bmatrix} \sigma_x \\ \sigma_y \\ \tau_{xy} \end{bmatrix} = T^{-1} \begin{bmatrix} \sigma_1 \\ \sigma_2 \\ \tau_{12} \end{bmatrix} = T^{-1} Q \begin{bmatrix} \varepsilon_1 \\ \varepsilon_2 \\ \gamma_{12} \end{bmatrix} = T^{-1} Q (T^{-1})^T \begin{bmatrix} \varepsilon_x \\ \varepsilon_y \\ \gamma_{xy} \end{bmatrix} = \bar{Q} \begin{bmatrix} \varepsilon_x \\ \varepsilon_y \\ \gamma_{xy} \end{bmatrix} \tag{7}$$

where  $\bar{Q}$  is the off-axis stiffness matrix of the lamina.

The laminate comprises multiple laminas, and the plies of the laminate are shown in Figure 4a. The in-plane strains of the laminate include mid-plane strains (normal strains  $\varepsilon_x^0$  and  $\varepsilon_y^0$ , and shear strain  $\gamma_{xy}^0$ ) and mid-plane curvatures (bending curvatures  $\kappa_x$  and  $\kappa_y$ , and torsion curvature  $\kappa_{xy}$ ). The internal forces ( $N_x$ ,  $N_y$ , and  $N_{xy}$ ) and internal moments ( $M_x$ ,  $M_y$ , and  $M_{xy}$ ) act on the unit width of the laminate cross-section with a thickness of  $h$ , as shown in Figure 4b. Hence, the internal force–strain relationship of the laminate can be expressed as:

$$\begin{bmatrix} N \\ M \end{bmatrix} = \begin{bmatrix} A & B \\ B & D \end{bmatrix} \begin{bmatrix} \varepsilon^0 \\ \kappa \end{bmatrix} \tag{8}$$

where  $A$ ,  $B$ , and  $D$  are the tensile, coupling, and bending stiffness matrices, respectively, and their coefficients can be obtained by integrating the off-axis stiffness coefficient,  $\bar{Q}_{ij}$ .  $N$  and  $M$  are the vectors of the internal force and moment, respectively.  $\varepsilon^0$  and  $\kappa$  are the vectors of strain and curvature, respectively.

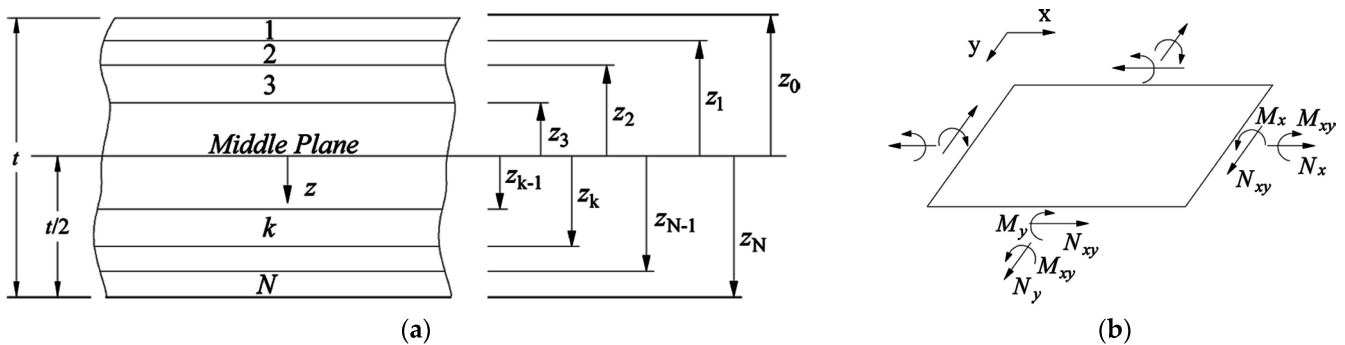


**Figure 4.** Laminate structure. (a) Plies of laminate and z-coordinate of laminas; (b) internal forces and moments of laminate in the plane stress state.

Regularizing the coefficients of the stiffness matrix in Equation (8) and inverting the matrix yields the following equation:

$$\begin{bmatrix} \varepsilon^0 \\ \kappa^* \end{bmatrix} = \begin{bmatrix} a^* & \frac{1}{3}\beta^* \\ \beta^{*T} & \delta^* \end{bmatrix} \begin{bmatrix} N^* \\ M^* \end{bmatrix} \tag{9}$$

When a uniaxial internal force  $N_x$  is applied to the laminate while the other internal forces and moments are zero, the normal strain  $\epsilon_x^0$  can be obtained by solving Equation (9), as follows:

$$\epsilon_x^0 = \alpha_{11}^* N_x \tag{10}$$

The  $x$ -direction elastic modulus of the laminate in the plane stress state is expressed as:

$$E_x^0 = \frac{1}{\alpha_{11}^*} \tag{11}$$

### 2.1.2. Helical Layers

Assume that the helical layer is the  $j$ th layer of the pipe. The helical layer comprises  $n_j$  spiral belts uniformly distributed along the circumferential direction; therefore, each spiral belt is subjected to the same tensile load. The fiber-direction tensile load on a single spiral belt can be expressed as follows:

$$F_{1(j)} = \sigma_{1(j)} A_{1(j)} = E_{1(j)} \epsilon_{1(j)} b_{(j)} t_{(j)} \tag{12}$$

where  $E_{1(j)}$  is the fiber-direction elastic modulus of GFRP;  $\epsilon_{1(j)}$  is the fiber-direction strain of the spiral belt;  $b_{(j)}$  and  $t_{(j)}$  are the width and thickness of the spiral belt, respectively; and the subscript  $j$  indicates the  $j$ th layer of the pipe.

As shown in Figure 5a, for the spiral belt with helix angle  $\alpha_j$ , the geometric relationship between the strain along the fiber and axial directions of the pipe can be expressed as follows:

$$\epsilon_{1(j)} = \frac{\Delta L_w}{L_w} = \frac{\Delta L \cos \alpha_{(j)}}{L / \cos \alpha_{(j)}} = \cos^2 \alpha_{(j)} \frac{\Delta L}{L} \tag{13}$$

where  $L_w$  denotes the initial length of the spiral belt corresponding to the pipe with length  $L$ , and  $\Delta L_w$  is the variation in the length of the spiral belt.

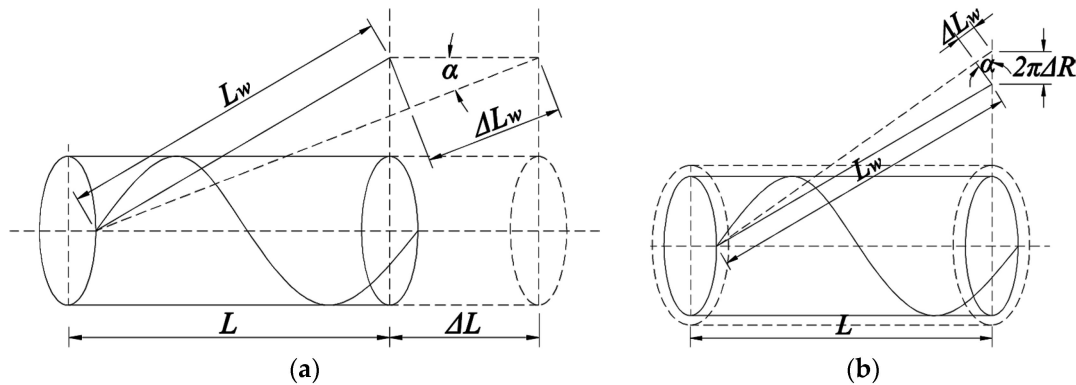


**Figure 5.** Deformation of spiral belts. (a) Deformation induced by axial strain of inner layers; (b) deformation induced by radial strain of inner layers.

Substituting Equation (12) into Equation (13), the relationship between the axial tensile load and axial strain of the spiral belt can be expressed as follows:

$$F_{(j)} = F_{1(j)} \cos \alpha_{(j)} = E_{1(j)} b_{(j)} t_{(j)} \cos^3 \alpha_{(j)} \frac{\Delta L}{L} \tag{14}$$

Under axial tensile loads, the pipe undergoes axial elongation and radial compression deformation. When the radial deformations of the inner layers are considered, the fiber-direction strains of the spiral belts change, which significantly affects the axial stiffness of the pipe. Based on Figure 5b, the geometric relationship between the fiber-direction strain

of the spiral belt with helix angle  $\alpha_j$  and the radial strain of the liner can be expressed as follows:

$$\varepsilon_{1(j)} = \frac{\Delta L_w}{L_w} = \frac{2\pi\Delta R \sin\alpha_{(j)}}{2\pi R / \sin\alpha_{(j)}} = \sin^2\alpha_{(j)} \frac{\Delta R}{R} \tag{15}$$

where  $R$  is the initial average radius of the liner, and  $\Delta R$  is the variation in  $R$ .

Assume that the ratio of the radial compression deformation to the axial elongation is the Poisson’s ratio of the liner material [6], i.e.,

$$\nu_{PE} = \frac{\Delta R_{(1)} / R_{(1)}}{\Delta L / L} \tag{16}$$

Subsequently, using Equations (13)–(16), the relationship between the axial tensile load and axial strain of the spiral belt, considering the radial compression deformation of the liner, can be expressed as follows:

$$F_{(j)} = F_{1(j)} \cos\alpha_{(j)} = E_{1(j)} b_{(j)} t_{(j)} \cos^3\alpha_{(j)} \left(1 - \nu_{PE} \tan^2\alpha_{(j)}\right) \frac{\Delta L}{L} \tag{17}$$

The structural layers of the unbonded flexible pipes are independent. Thus, the axial tensile load applied to the entire pipe is equal to the sum of the axial tensile load acting on each layer. Due to the same end constraints, the axial elongation of each layer is the same. Therefore, the total axial tensile stiffness of the fiber-reinforced flexible pipe can be obtained by summing the axial tensile stiffness of each layer. Based on Equations (1) and (17), the total axial tensile stiffness of the pipe can be expressed as follows:

$$(EA)_{total} = \sum_{i=1,2,6,9} E_{(i)} A_{(i)} + \sum_{j=3,4,5,7,8} n_{(j)} E_{1(j)} b_{(j)} t_{(j)} \cos^3\alpha_{(j)} \left(1 - \nu_{PE} \tan^2\alpha_{(j)}\right) \tag{18}$$

As shown in Equation (18), the winding angles of spiral layers have significant effects on the axial stiffness of fiber-reinforced flexible pipes.

### 2.2. Numerical Model

A 3D numerical model was established using the finite element software ABAQUS to simulate the axial tensile behavior of a fiber-reinforced flexible pipe with an inner diameter of 150 mm and a length of 2700 mm. The main geometric parameters of the sample and the material parameters obtained by mechanical properties tests are listed in Tables 2 and 3 [32], respectively.

**Table 2.** Geometric parameters and materials of the pipe.

Layer	Thickness (mm)	Winding Angle (°)	Number of Belts	Materials
Liner (L1)	8	–	–	PE
Inner hoop layer (L2)	2	±80	–	GFRP1
Inner tensile reinforcement layer 1 (L3)	2.5	54	20	GFRP2
Inner tensile reinforcement layer 2 (L4)	2.5	–54	20	GFRP2
Hoop reinforcement layer (L5)	8.5	86	2	GFRP2
Membrane (L6)	4	–	–	PE
Outer tensile reinforcement layer 1 (L7)	3	30	36	GFRP2
Outer tensile reinforcement layer 2 (L8)	3	–30	36	GFRP2
Outer sheath (L9)	4	–	–	PE

**Table 3.** Parameters of materials.

Parameters	GFRP1	GFRP2	PE
$E_1$ (GPa)	33.70	49.6	1.1
$E_2$ (GPa)	7.35	1.46	–
$G_{12}$ (GPa)	2.50	2.7	–
$\nu_{12}$	0.3	0.27	0.45
$\rho$ (g/cm <sup>3</sup> )	2.1	2.1	0.95

Local coordinate systems were established to define the material orientations for all fiber reinforcement layers, wherein directions 1, 2, and 3 referred to the fiber, transverse, and thickness directions, respectively; thus, the output of strain and stress followed the direction of the local coordinates. Two reference points, RP1 and RP2, were set at the center points of the two end sections, and kinematic coupling constraints were established between the two points and the corresponding surfaces; thus, boundary conditions and concentrated loads were applied to the model via the reference points. All degrees of freedom of RP1 and the axial torsion degrees of freedom (UR3) of RP2 were constrained, as shown in Figure 6a. The contacts between different layers and different spiral belts were defined as general contacts. The normal behavior was set as hard contact, whereas the tangential behavior was defined using a penalty method based on the Coulomb friction model. Friction tests were performed to measure the friction factors between the samples of GFRP and PE using a peel testing machine. Based on the results of the friction tests, the friction factor between the GFRP layers was set to 0.18, whereas that between the GFRP and PE layers was set to 0.08.

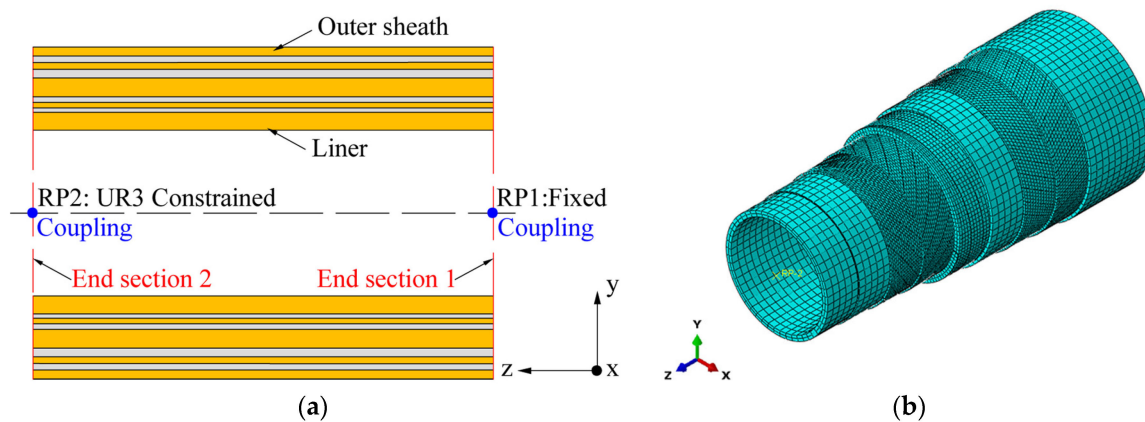


**Figure 6.** Finite element model of glass fiber-reinforced flexible pipe. (a) Couplings and boundary conditions; (b) meshes of the model.

Structured meshes were employed for the cylindrical layers, while swept meshes were adopted along the helix direction for the helical layers. Mesh size sensitivity analyses were performed to determine the mesh sizes of different layers. In the first set of models, the initial global mesh sizes of the cylindrical layers were set as 10 mm, and those of helical layers were set as 8, 7, 6, 5 and 4 mm, respectively. In the second set of models, the initial global mesh sizes of the helical layers were set as 5 mm, and those of the cylindrical layers were set as 13, 12, 11, 10 and 9 mm, respectively. Figure 7 illustrates the results of axial displacements obtained by different models. According to the results, the global mesh sizes of the cylindrical and helical layers were set as 10 and 5 mm, respectively. The mesh numbers along the circumferential and thickness directions of L1 were set as 50 and 2, respectively. The mesh numbers along the circumferential and thickness directions of L9 were set as 70 and 2, respectively. The mesh numbers along the transverse and thickness directions of the spiral belts of L5 were set as 50 and 2, respectively. The mesh number

along the transverse direction of each spiral belt of the tensile reinforcement layers was set as 4. To avoid the effect of excessive deformation on the analysis, the C3D8R element was adopted for all parts of the model, and the enhanced hourglass control mode was selected to limit the hourglass expansion. The entire model comprised 622,928 elements and 1332,258 nodes, as shown in Figure 6b.

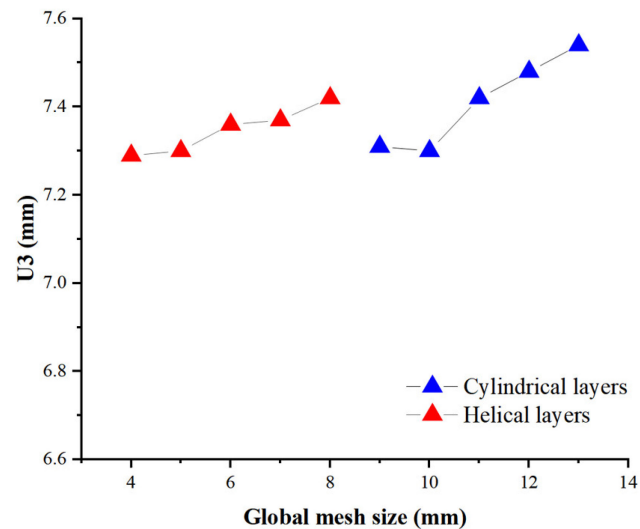


**Figure 7.** The axial displacements of the pipe obtained by numerical models with different global mesh sizes.

The ABAQUS/Explicit solver was employed in the quasi-static analysis to prevent convergence problems caused by nonlinear factors, such as complex contacts. The loading time was set to 0.1 s, and a concentrated load of 300 kN in the U3 direction was applied on End Section 2 through RP2. To avoid the effect of inertia, a smooth step was used to control the loading rate, and the energy curves were monitored during the loading process. Geometric nonlinearity was also adopted in the model to ensure the accuracy of the calculation results.

### 2.3. Prototype Test

A full-scale axial tensile test was performed on a glass-fiber-reinforced unbonded flexible pipe with an inner diameter of 150 mm. During the test, the ends of the sample were connected to the testing machine through end fittings. The end fittings were sufficiently long to prevent the pipe from slipping under large axial tensile loads. The presence of end fittings resulted in high-stress regions near the ends. To avoid the effect of stress concentration, the effective length (the total length minus the lengths of the end fittings) of the sample should not be less than twice the maximum pitch of the spiral belts, based on specifications [3,4]. The maximum pitch of the spiral belts in this sample was 1180 mm, and the total and effective lengths of this sample were 4500 and 2700 mm, respectively.

The sample was connected to a horizontal tensile-testing machine. One end was completely fixed on the support of the machine, and the other end was connected to a hydraulic actuator with restricted axial torsion. Two sections of the sample, S1 and S2, were selected to monitor the strain; here, S1 was the midspan section, S2 was located between S1 and the fixed end, and the distance between S1 and S2 is 500 mm, as shown in Figure 8a,b. S1 was the main section for the measurement of fiber-direction strains of spiral belts, and S2 was selected for comparative analysis. A section of the outer sheath with a width of 15 cm was removed from S1 and S2; thus, the spiral belts of the outer tensile reinforcement layer were exposed. Additionally, strain gauges were attached, as shown in Figure 8c.

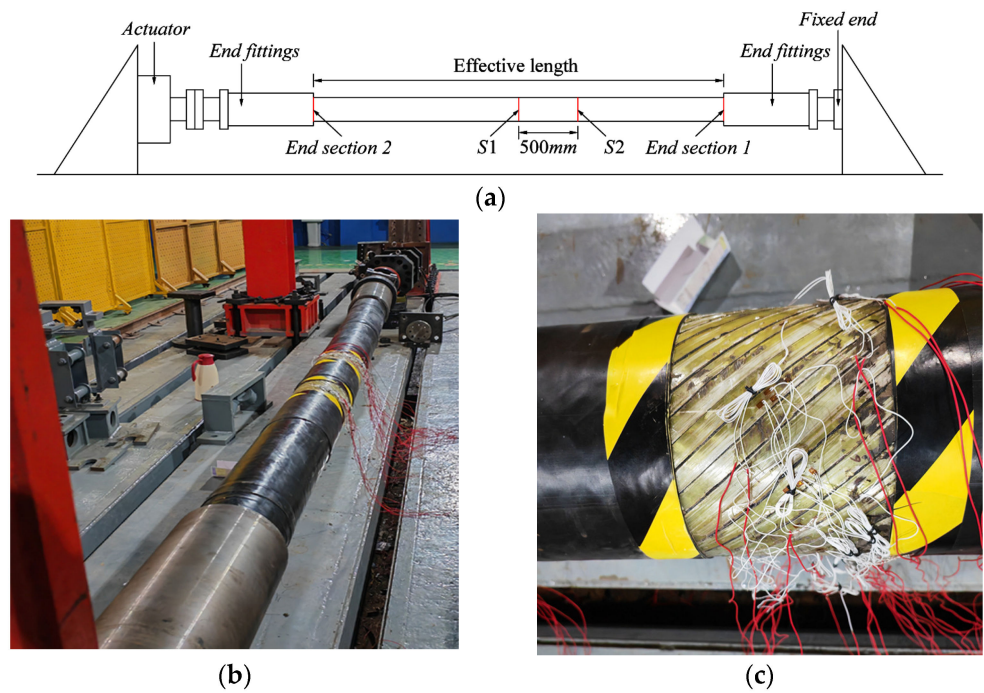


**Figure 8.** Axial tensile test. (a) positions of measuring sections; (b) testing machine and sample; (c) strain gauges on the spiral belts.

The spiral belts were symmetrically distributed in the circumferential direction; thus, the points on the spiral belts (nos. 1-4) at positions  $0^\circ$ ,  $45^\circ$ ,  $90^\circ$  and  $180^\circ$  along the circumferential directions of S1 and S2, respectively, were selected as the main measurement points, as shown in Figure 9a. Three strain gauges were attached along the fiber direction in the middle position of each of the four belts to decrease the measurement errors, as shown in Figure 9b. For S1, one strain gauge was attached along the fiber direction in the middle of each of the other belts (nos. 5-10).

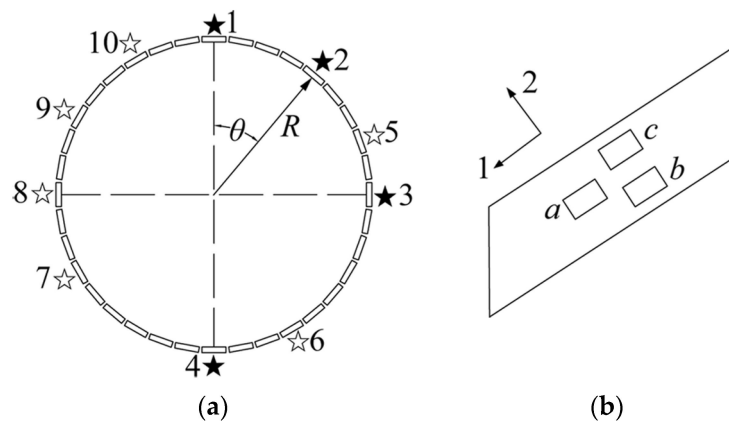


**Figure 9.** Positions of spiral belts and strain gauges. (a) positions and numbers of spiral belts in circumferential direction; (b) positions of strain gauges on spiral belt.

Four loading–unloading cycles were applied on End Section 2 using a computer-controlled actuator, and the amplitudes of the tensile loads in the four loading processes were 210, 205, 197, and 105 kN, respectively. Slow loading processes were performed to avoid inertial effects; thus, the loading rate was controlled at approximately 1.35 kN/m, and the total testing time was 1036 s. The value of the tensile load can be measured using a force sensor, and the value of the strain can be obtained using a data acquisition instrument.

### 3. Results and Discussions

#### 3.1. Energy Time History Curves

The time history curves of ALLIE, ALLSE, ALLAE, and ALLKE were extracted from the finite element results, as shown in Figure 10a. The internal energy curve is relatively smooth without evident fluctuations during the entire loading process, and the kinetic and artificial strain energies remain low. At 0.058 s, the ratio of the peak value of the kinetic energy to the corresponding internal energy is only 1.7%, which satisfies the quasi-static condition. At 0.1 s, the ratio of the artificial strain energy to the internal energy is approximately 2.9%, which confirms that the hourglass problem does not significantly affect the results. At 0.1 s, the ratio of the elastic strain energy to the internal energy is 97.1%, which indicates that almost all the work yielded by the tensile load is converted into the elastic strain of the pipe. Therefore, the contributions of different layers to the axial load capacity can be illustrated directly using the strain energy curves.

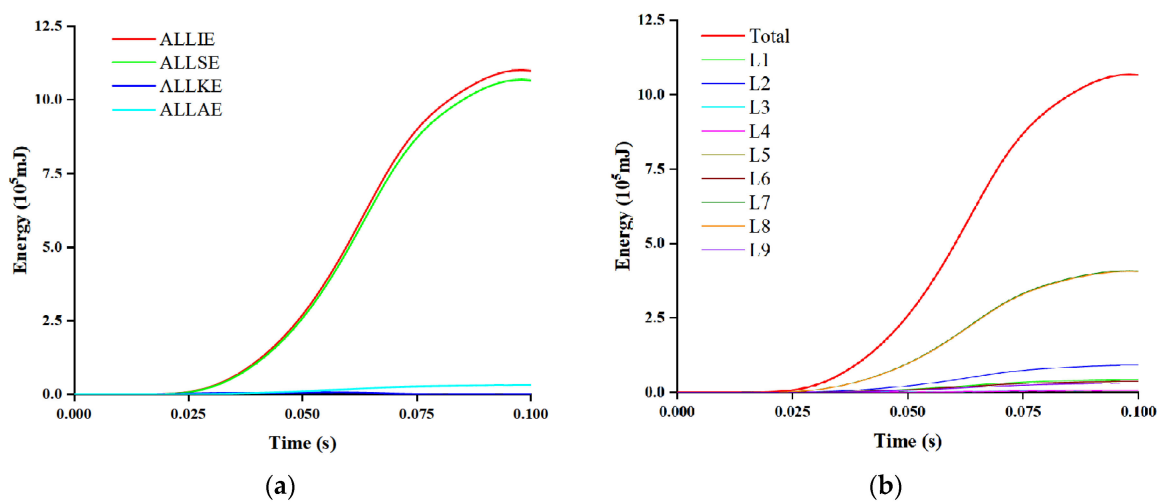


**Figure 10.** Energy history curves of finite element model. (a) Comparisons of different energy; (b) comparisons of strain energy of different layers.

Figure 10b and Table 4 show the values of the elastic strain energy of different layers and the entire pipe. As shown, the strain energy of Layers L7 and L8 constitutes 38.34% and 38.04% of the total strain energy, respectively. As can be inferred from Equations (13) and (15), the strain of Layer L7 is slightly larger than that of Layer L8 because the radius of Layer L7 is smaller than that of Layer L8 and the two layers share the same elastic constants, which leads to a larger strain energy in Layer L7. The contribution ratio of the strain energy of the two layers is 76.42%, which shows that the outer tensile reinforcement layers with a winding angle of 30° contribute the most to the axial load capacity. However, the strain energy of the inner tensile reinforcement layers with a winding angle of 54° constitutes only 1.19% of the total strain energy, which shows that these layers do not significantly affect the axial load capacity. These results indicate that the winding angle of fibers have a significant effect on the axial load capacity of the spiral belts and that a relatively small winding angle is more conducive for the pipe to resist axial load. The PE layers also contribute to the axial load capacity of the pipe. The contribution ratio of the strain energy of the inner layer (4.03%) is greater than that of the membrane (3.45%) and outer sheath (2.87%) owing to the effect of position and thickness. The inner hoop layer with a large winding angle and small thickness contributes to 8.51% of the total strain energy, which is second only to that of the outer tensile reinforcement layers and significantly higher than that of the other cylindrical layers, for the reason that it is completely cylindrical and the equivalent elastic modulus along the axis of the pipe is 6.5 times that of the PE layer. Although the

thickness is large, the hoop reinforcement layer is a helical structure instead of a completely cylindrical structure; thus, it contributes to only 3.50% of the total strain energy.

**Table 4.** Strain energy and contribution ratio of different layers.

Layer	L1	L2	L3	L4	L5	L6	L7	L8	L9	Total
Strain energy (10 <sup>5</sup> mJ)	0.43	0.91	0.07	0.06	0.37	0.37	4.09	4.06	0.31	10.67
Contribution ratio (%)	4.03	8.51	0.64	0.55	3.50	3.45	38.34	38.08	2.87	100

**3.2. Strain Distribution of Outer Tensile Reinforcement Layer**

Figure 11 illustrates the fiber-direction strain in Sections S1 and S2 of the outer tensile reinforcement layer (Layer L8). The maximum and minimum strains of S1 are 0.179% and 0.131%, respectively, and those of S2 are 0.180% and 0.132%, respectively. Due to the coupling effect of tension and torsion in the spiral wound structure, local bending and torsion deformation will occur in the spiral belts when the pipe is subjected to tensile load; thus, the strains could not be completely uniform along the transverse direction of the belts. The strains at the middle positions are higher than those at the edges in the transverse direction of the spiral belts.

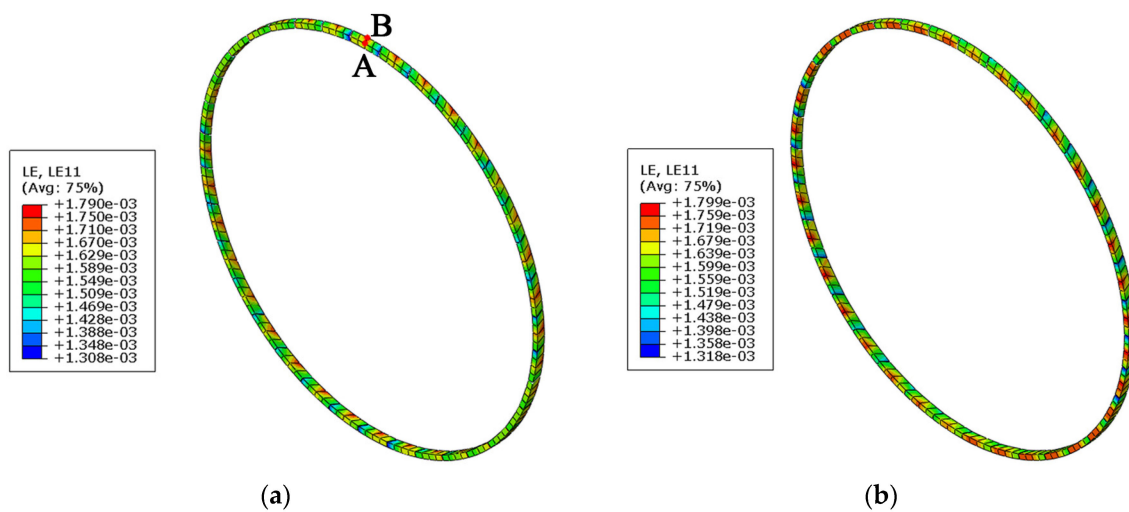


**Figure 11.** Fiber-direction strains of Layer L8. (a) Strains of S1; (b) Strains of S2.

For the spiral belt at the 0° position along the circumferential direction of S1, the fiber-direction strain was obtained by averaging the fiber-direction strains of Points A and B (as shown in Figure 10a) at the middle position of the spiral belt. In Section S1, one spiral belt was selected from every three spiral belts along the circumferential direction from the 0° position to extract the strain data; thus, the fiber-direction strains of 12 spiral belts were obtained. Similarly, the fiber-direction strains of the 12 spiral belts selected in S2 were obtained. The average values of the fiber-direction strain of the spiral belts in S1 and S2 are 0.1712% and 0.1695%, respectively, as shown in Figure 12.

The fiber-direction strains of S1 and S2 were obtained by averaging the values of the fiber-direction strain of the spiral belts measured by strain gauges in the prototype tests. When the amplitude of tensile load reaches 210 kN, the fiber-directions strains of S1 and S2 are 0.111% and 0.103%, respectively, as shown in Figure 13. The relationships between the strains in the fiber direction of S1 and S2 obtained by test and axial tensile loads are near-linear, even though four loading–unloading cycles were performed in the test, which indicates that the deformation of the pipe is still in the linear elastic range; thus, the strain per unit load of each section can be obtained by linear fitting. When the amplitude of tensile load reaches 300 kN, the fiber-direction strains of S1 and S2 are 0.171%

and 0.169%, respectively. The relationships between the strains in the fiber direction of S1 and S2 obtained by the numerical model using smooth step are also near-linear. The finite element and test results of the fiber-direction strain under the unit load of the spiral belts in Section S1 are  $6.0157 \times 10^{-4}/\text{kN}$  and  $6.1233 \times 10^{-4}/\text{kN}$ , respectively, and the finite element result is 1.8% lower than the test result (see Table 5). The finite element and test results of the fiber-direction strain under a unit load of the spiral belts in S2 are  $5.9798 \times 10^{-4}/\text{kN}$  and  $5.7496 \times 10^{-4}/\text{kN}$ , respectively, and the finite element result is 4.0% greater than the test result. The errors between the numerical and experimental results of the two sections are insignificant, which indicates the high accuracy of the finite element model.

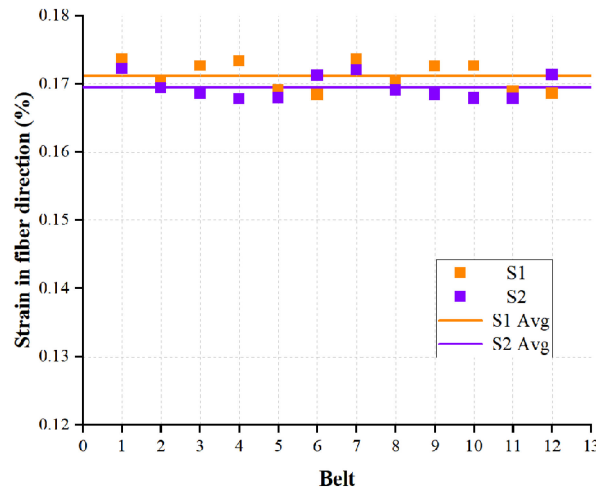


Figure 12. Fiber-direction strains of spiral belts at S1 and S2 of Layer L8.

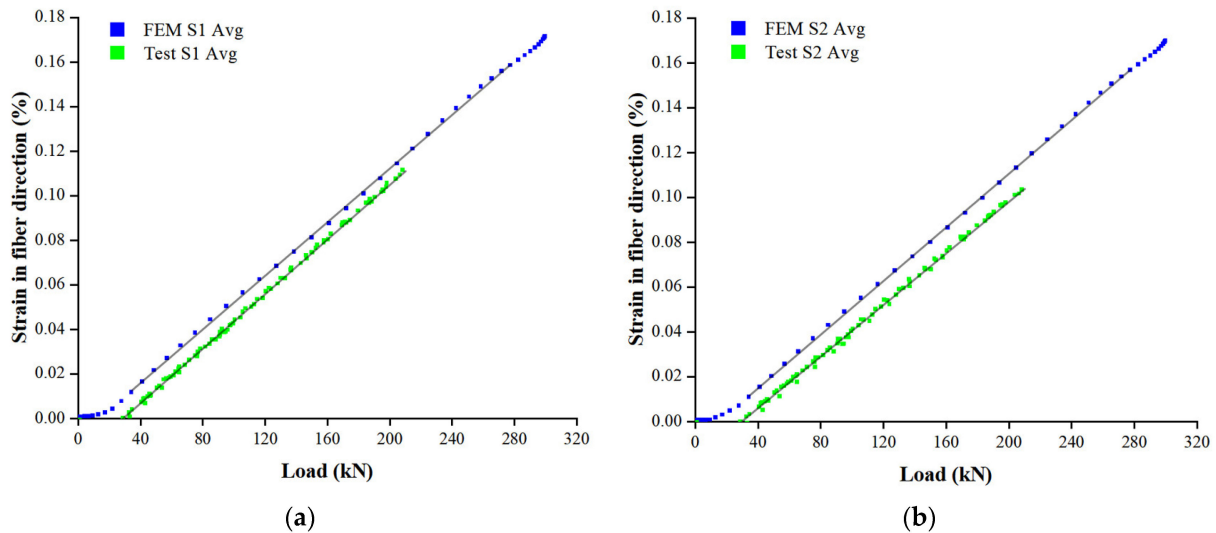


Figure 13. Strain-load curves of spiral belts in Layer L8. (a) curves of S1; (b) curves of S2.

Table 5. Mean fiber-direction strains of spiral belts under unit load.

Sections	Test Results ( $\times 10^{-4}/\text{kN}$ )	Numerical Results ( $\times 10^{-4}/\text{kN}$ )	Errors (%)
S1	6.0157	6.1233	1.8
S2	5.9798	5.7496	4.0

### 3.3. Distribution of Stress in Different Layers

Figure 14 illustrates the distribution of the von Mises stress in the pipe sections. The maximum von Mises stress (116.5 MPa) at the end section is 28.9% higher than that at the midspan section (90.5 MPa), which demonstrates the end effect of the pipe. The von Mises stresses in the outer tensile reinforcement layers are significantly higher than those in the other layers, which confirms that the outer tensile reinforcement layers contribute significantly to the axial load capacity of the pipe.

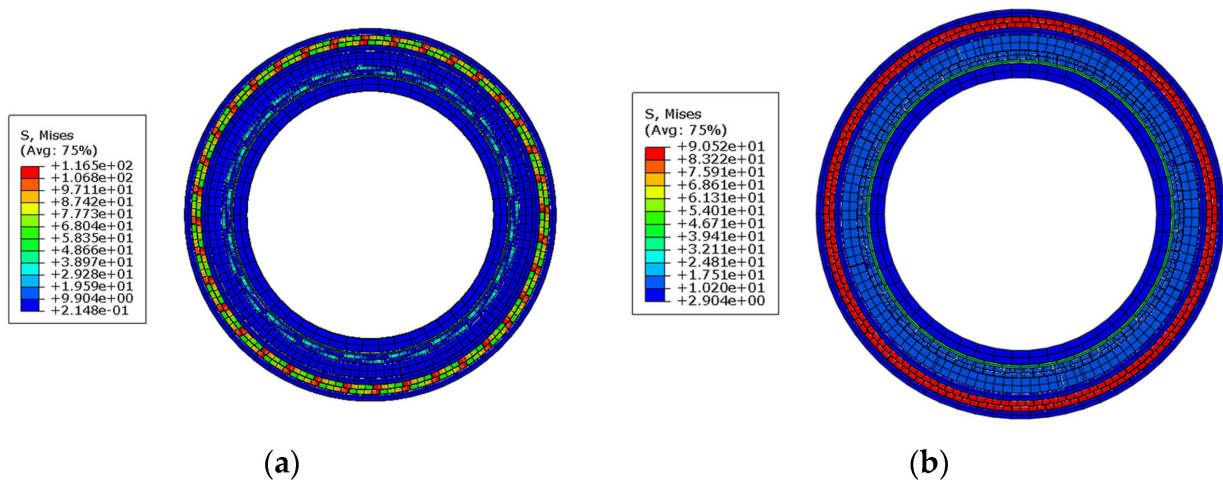
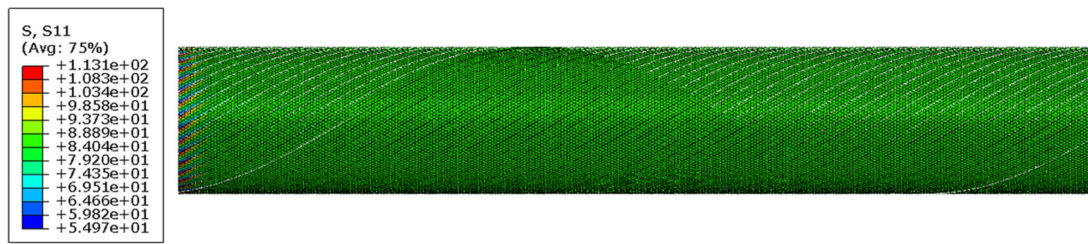


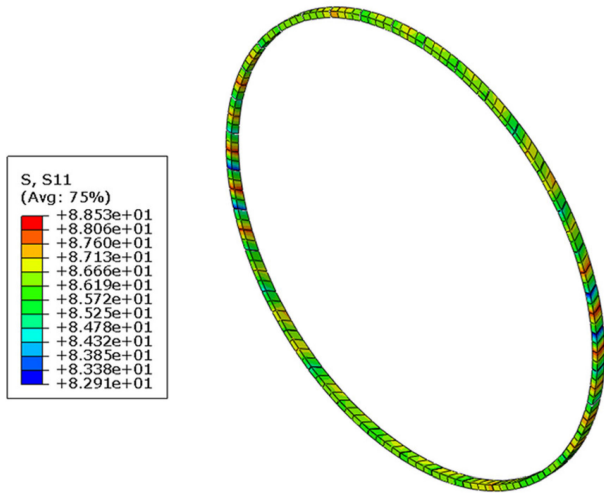
Figure 14. Mises stresses of the pipe. (a) end section; (b) midspan section.

Figure 15 illustrates the distribution of the fiber-direction stress at different positions in the outer tensile spiral layer (Layer L8). As shown in Figure 15a, the variation in the fiber-direction stress of the outer tensile spiral belts along the axis of the pipe is not significant, except at the end sections. As shown in Figure 15b, the distribution of the fiber-direction stress along the circumferential direction of S1 (corresponding to S1 selected in the test) is relatively uniform, with a maximum value of 88.5 MPa and a minimum value of 82.9 MPa. The stresses at the middle positions are slightly higher than those at the edges in the transverse direction of the spiral belts. As shown in Figure 15c, the maximum and minimum values of the fiber-direction stress of the spiral belts in S2 (corresponding to S2 selected in the test) are 88.2 and 83.2 MPa, respectively, and the stress distribution is similar to that of Section S1.

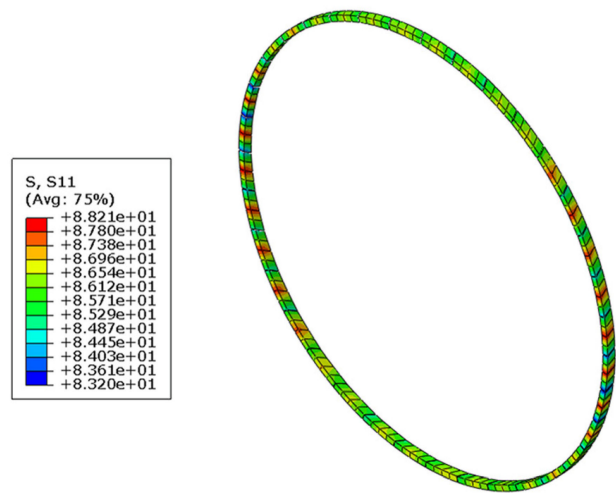
Figure 16 illustrates the distribution of the fiber-direction stress at different positions in the outer tensile spiral layer (Layer L7). As shown in the figure, the stress distributions of the two sections are similar to those of the corresponding sections of Layer L8. The same method as described in Section 3.2 was employed to calculate the mean fiber-direction stress of 12 spiral belts at the midspan section of Layers L8 and L7. The relationships between the mean fiber-direction stress and axial tensile load are shown in Figure 17. The figure illustrates that, as the axial tensile load increases, the mean fiber-direction stresses of the spiral belts increase approximately linearly. When the axial tensile load reaches 300 kN, the fiber-direction stresses of Layer L7 and L8 are 88.57 and 87.19 MPa, respectively. The stress of Layer L7 is slightly higher than that of Layer L8, indicating that Layer L7 contributes more to the axial load capacity than Layer L8, which is similar to the conclusion presented in Section 3.1.



(a)

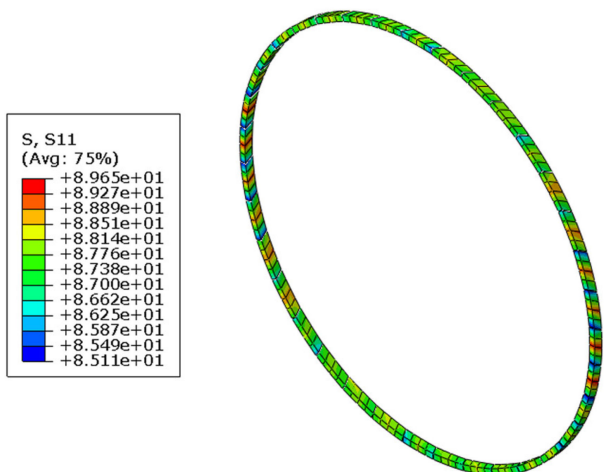


(b)

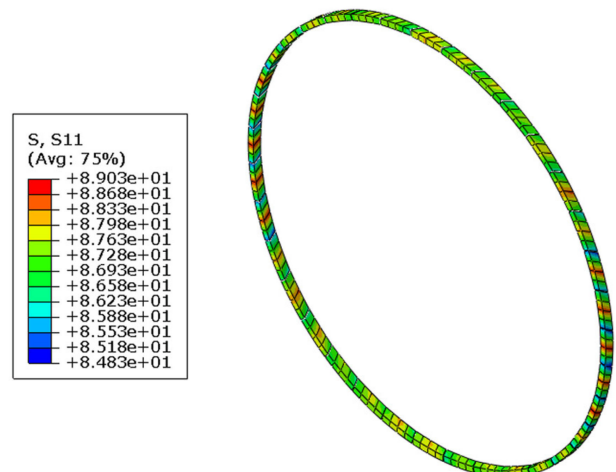


(c)

Figure 15. Distribution of fiber-direction stresses of Layer L8. (a) From end section to midspan; (b) S1; (c) S2.

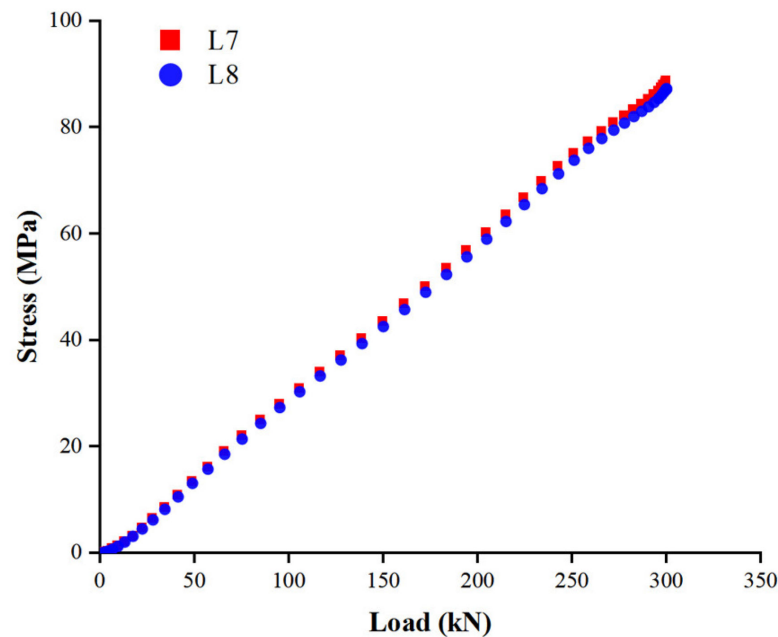


(a)



(b)

Figure 16. Distribution of fiber-direction stresses of Layer L7. (a) Section S1; (b) Section S2.



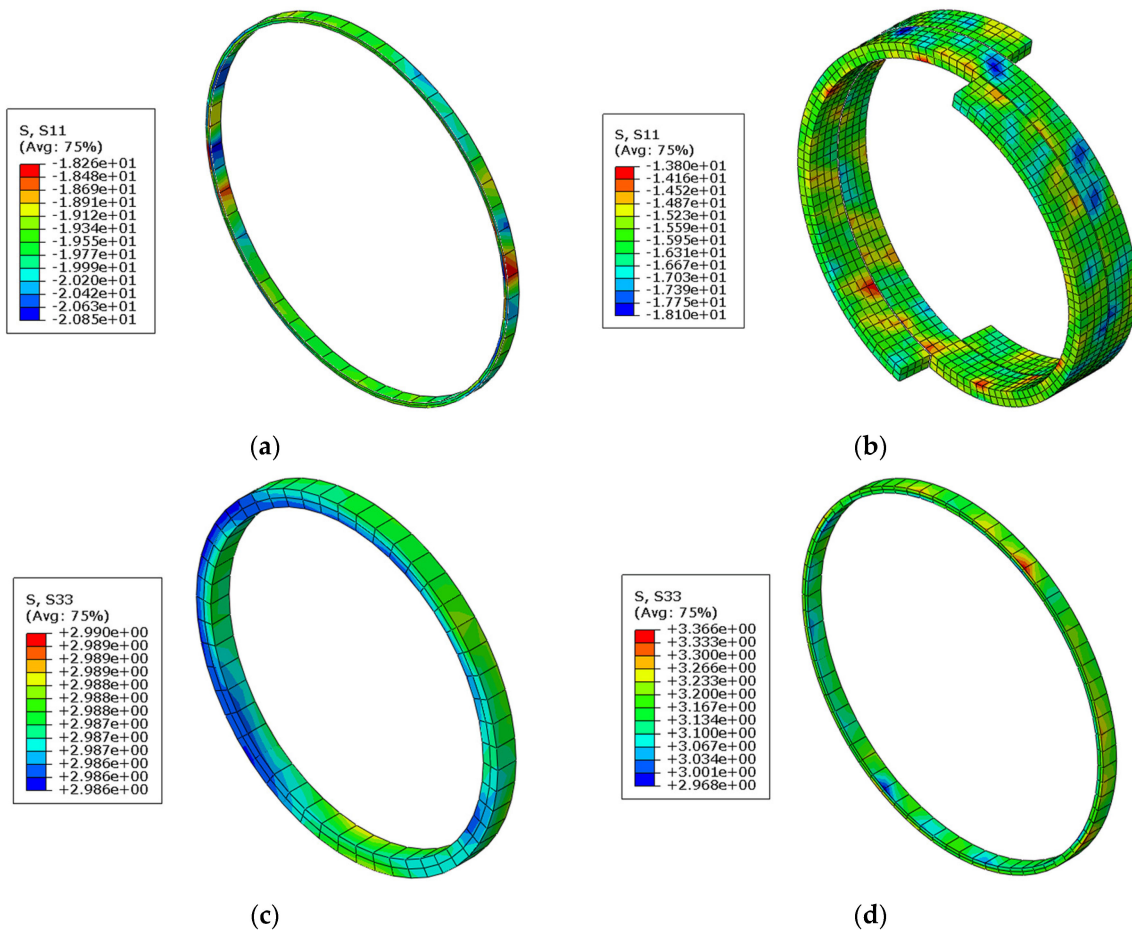
**Figure 17.** The mean fiber-direction stresses of the spiral belts in the midspan sections of the outer tensile reinforcement layers under the axial tensile loads.

Figure 18 illustrates the stress distribution in the midspan sections of the different layers. The inner hoop layer was subjected to compressive stress along the fiber direction, and the maximum and minimum values of the fiber-direction stress at the midspan section are 20.8 and 18.3 MPa, respectively (see Figure 18a). Similarly, the hoop reinforcement layer was subjected to compressive stress along the fiber direction, and the maximum and minimum values of the fiber-direction stress at the midspan section are 18.1 and 13.8 MPa, respectively (see Figure 18b). The inner hoop and hoop reinforcement layers are the main carriers of radial load, and their filament winding angles are  $80^\circ$  and  $86^\circ$ , respectively, which are close to the circumferential direction of the pipe; thus the compressive stress along the fiber direction reflects the radial compression of the pipe under axial tensile load. The maximum axial stress at the midspan section of the liner and outer sheath are 2.99 and 3.37 MPa, respectively (see Figure 18c,d), which indicates that the contributions of the two layers to the axial load capacity are limited.

### 3.4. Axial Tensile Stiffness of the Pipe

The axial displacement U3 of reference point RP1 of the numerical model was extracted to obtain the axial load–strain relationship of the pipe, as shown in Figure 19; thus, the axial tensile stiffness of the pipe can be obtained via linear fitting. Additionally, Equation (18) was used to calculate the axial tensile stiffness of the pipe. In analytical model 1, the radial compression of the pipe was considered; thus,  $\nu_{PE} = 0.45$ . In analytical model 2, the radial compression of the pipe was not considered; thus,  $\nu_{PE} = 0$  (Equation (18)).

The axial stiffnesses of the pipe obtained using analytical models 1 and 2 are 2.5% and 29.2% higher than that of the numerical model, respectively (see Table 6). This indicates that the analytical model, which considers radial compression, yields more accurate results of the axial tensile stiffness of the pipe, whereas the analytical model, which does not consider radial compression, yields a much larger axial tensile stiffness.



**Figure 18.** Distribution of stresses at midspan section of different layers. (a) Inner hoop layer; (b) hoop reinforcement layer; (c) liner; (d) outer sheath.

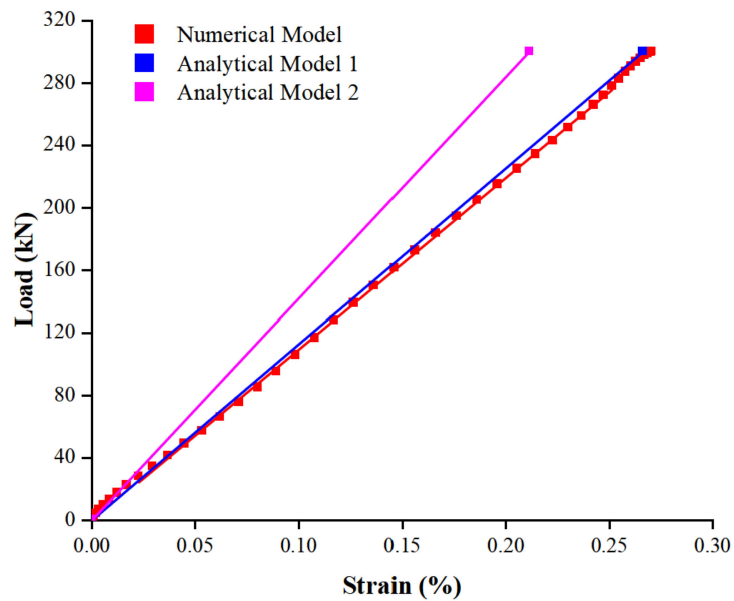


**Figure 19.** Axial load–strain relationships of fiber-reinforced flexible pipe.

**Table 6.** Axial tensile stiffness of fiber-reinforced flexible pipe obtained using different methods.

Models	Tensile Stiffness ( $\times 10^5$ kN)	Errors (%)
Numerical	1.0985	–
Analytical 1	1.1262	2.5
Analytical 2	1.4192	29.2

#### 4. Conclusions

In this study, the mechanical characteristics of a glass fiber-reinforced flexible pipe under an axial tensile load were investigated using analytical, numerical, and experimental methods. Based on the load–strain relationship of different layers, analytical equations considering the anisotropy of the material and the effect of radial compression deformation were derived to calculate the axial tensile stiffness of the pipe. A 3D numerical model was established to simulate the axial tensile behavior of the pipe; thus, the distributions of strain and stress in different layers and the axial displacement of the pipe were obtained. An axial tensile test was performed to measure the fiber-direction strains of the multiple spiral belts in two sections of the pipe. Based on a comparative analysis of the results of different methods, the following conclusions were inferred:

1. The winding angle significantly affected the axial load capacity of the spiral belts in the tensile reinforcement layers because the stiffness of GFRP is mainly provided by fibers. A smaller winding angle is more conducive to the axial load capacity.
2. The errors between the results of the average fiber-direction strains of the outer tensile reinforcement layer in Sections S1 and S2 by the numerical model and test are insignificant, which indicates the high accuracy of the finite element model.
3. The distribution of the fiber-direction stress in Layer L8 is relatively uniform along the axial and circumferential directions of the pipe, except for the regions near the end sections. The inner hoop and hoop reinforcement layers are subjected to compressive stress in the fiber direction, which indicates the radial compression effect of the pipe under an axial tensile load.
4. The result of axial tensile stiffness calculated by the analytical model considering radial compression is very close to that obtained by the numerical model; thus, the accuracy of analytical model is proved.

In summary, the analytical model considering the radial compression of the pipe has high accuracy in predicting the axial tensile stiffness of fiber-reinforced flexible pipes. The finite element model can also provide accurate descriptions of the distribution characteristics of strain and stress. Nevertheless, the analytical and numerical models proposed in this study can only be used for the elastic deformation range of fiber-reinforced flexible pipes. When the pipe is subjected to a larger axial tensile load, the spiral belts may rupture or other damage may occur. In future studies, the ultimate strength of GFRP should be considered such that the tensile failure behavior of fiber-reinforced flexible pipes can be investigated.

**Author Contributions:** Conceptualization, Z.S.; Investigation, W.H. and H.L.; Methodology, Z.S.; Supervision, W.H. and H.L.; Data curation, Investigation, Z.S.; Formal analysis, Z.S.; Experiment, Z.S., Y.B., Y.Y., S.W. and Y.F.; Writing—original draft, Z.S.; Writing—review and editing, W.H. and H.L. All authors have read and agreed to the published version of the manuscript.

**Funding:** This research was funded by the National Key R&D Program of China (2021YFA1003501), the National Natural Science Foundation of China (No. U1906233, 11732004, 52201312), and the Key R&D Program of Shandong Province (2019JZZY010801).

**Institutional Review Board Statement:** Not applicable.

**Informed Consent Statement:** Not applicable.

**Data Availability Statement:** Not applicable.

**Conflicts of Interest:** The authors declare no conflict of interest.

## References

- Do, A.T.; Lambert, A. Qualification of Unbonded Dynamic Flexible Riser with Carbon Fibre Composite Armours. In Proceedings of the Offshore Technology Conference, Houston, TX, USA, 30 April–3 May 2012.
- Bryant, M.; Bhat, S.; Chen, B. Nonmetallic Unbonded Flexible Pipes for Deep Water. In Proceedings of the 2007 International Oil Conference and Exhibition, Veracruz, Mexico, 27–30 June 2007.
- API. API SPEC 17J; Specification for Unbonded Flexible Pipe. API Publishing Services: Washington, DC, USA, 2014.
- API. API RP 17B; Recommend Practice for Flexible Pipe. API Publishing Services: Washington, DC, USA, 2014.
- De Oliveira, J.G.; Goto, Y.; Okamoto, T. Theoretical and Methodological Approaches to Flexible Pipe Design and Application. In Proceedings of the Offshore Technology Conference, Houston, TX, USA, 6–9 May 1985.
- Lu, Q.; Yue, Q.; Tang, M.; Zheng, J.; Yan, J. Reinforced Design of an Unbonded Flexible Flowline for Shallow Water. In Proceedings of the ASME 2010 29th International Conference on Ocean, Offshore and Arctic Engineering, Shanghai, China, 6–11 June 2010.
- Yue, Q.; Lu, Q.; Yan, J.; Zheng, J.; Palmer, A. Tension Behavior Prediction of Flexible Pipelines in Shallow Water. *Ocean Eng.* **2013**, *58*, 201–207. [\[CrossRef\]](#)
- Tang, M.; Yan, J.; Wang, Y.; Yue, Q. Tensile Stiffness Analysis on Ocean Dynamic Power Umbilical. *Chin. Ocean Eng.* **2014**, *28*, 259–270. [\[CrossRef\]](#)
- Wang, H.; Yang, Z.; Yan, J.; Wang, G.; Shi, D.; Zhou, B.; Li, Y. Prediction Method and Validation Study of Tensile Performance of Reinforced Armor Layer in Marine Flexible Pipe/Cables. *J. Mar. Sci. Eng.* **2022**, *10*, 642. [\[CrossRef\]](#)
- Bahtui, A.; Bahai, H.; Alfano, G. A Finite Element Analysis for Unbonded Flexible Risers under Axial Tension. In Proceedings of the ASME 27th International Conference on Offshore Mechanics and Arctic Engineering, Estoril, Portugal, 15–20 June 2008.
- Merino, H.E.M.; de Sousa, J.R.M.; Magluta, C.; Roitman, N. On the Coupled Extensional-Torsional Response of Flexible Pipes. In Proceedings of the ASME 2009 28th International Conference on Ocean, Offshore and Arctic Engineering, Honolulu, HA, USA, 31 May–5 June 2009.
- Ren, S.; Tang, W.; Guo, J. Behavior of Unbonded Flexible Risers Subject to Axial Tension. *Chin. Ocean Eng.* **2013**, *28*, 249–258. [\[CrossRef\]](#)
- Ramos, R.J.; Martins, C.A.; Pesce, C.P.; Roveri, F.E. A Case Study on the Axial-Torsional Behavior of Flexible Risers. In Proceedings of the ASME 27th International Conference on Offshore Mechanics and Arctic Engineering, Estoril, Portugal, 15–20 June 2008.
- Lopes, D.; Souza, I.; Falcao, G.; Clevelario, J.; Sheldrake, T. Analysis of Stress Levels and Indication of Ruptures of Flexible Pipes Tensile Armor Wires during a Fatigue Dynamic Tension to Tension Test. In Proceedings of the ASME 2012 31st International Conference on Ocean, Offshore and Arctic Engineering, Rio de Janeiro, Brazil, 1–6 July 2012.
- Bai, Y.; Liu, T.; Ruan, W.; Chen, W. Mechanical Behavior of Metallic Strip Flexible Pipe Subjected to Tension. *Comp. Struct* **2017**, *170*, 1–10. [\[CrossRef\]](#)
- Chen, W.; Xiong, H.; Bai, Y. Failure Behavior Analysis of Steel Strip—Reinforced Flexible Pipe under Combined Tension and Internal Pressure. *J. Therm. Comp. Mat.* **2020**, *33*, 727–753. [\[CrossRef\]](#)
- Liu, J.; Vaz, M.; Chen, R.; Duan, M.; Hernandez, I. Axial Mechanical Experiments of Unbonded Flexible Pipes. *Petr. Sci.* **2020**, *17*, 1400–1410. [\[CrossRef\]](#)
- Dong, L.; Zhang, Q.; Huang, Y.; Liu, G.; Li, Z. End Fitting Effect on Stress Evaluation of Tensile Armor Tendons in Unbonded Flexible Pipes Under Axial Tension. *J. Offsh Mech. Arct. Eng.* **2018**, *140*, 051701. [\[CrossRef\]](#)
- Dong, L.; Huang, Y.; Dong, G.; Zhang, Q.; Liu, G. The Tensile Armour Behaviour of Unbonded Flexible Pipes Close to End Fittings under Axial Tension. *Ship Offsh Struct.* **2016**, *11*, 445–460. [\[CrossRef\]](#)
- Nassiraei, H.; Rezadoost, P. Stress Concentration Factors in Tubular T/Y-Joints Strengthened with FRP Subjected to Compressive Load in Offshore Structures. *Int. J. Fat.* **2020**, *140*, 105719. [\[CrossRef\]](#)
- Zhu, X.; Lei, Q.; Meng, Y.; Cui, X. Analysis of Tensile Response of Flexible Pipe with Ovalization under Hydrostatic Pressure. *Appl. Ocean Res.* **2021**, *108*, 102451. [\[CrossRef\]](#)
- De Sousa, J.R.M.; Campello, G.C.; Kwietniewski, C.E.F.; Ellwanger, G.B.; Strohaecker, T.R. Structural Response of a Flexible Pipe with Damaged Tensile Armor Wires under Pure Tension. *Mar. Struct.* **2014**, *39*, 1–38. [\[CrossRef\]](#)
- Zhu, X.; Lei, Q.; Meng, Y.; Cui, X. Tensile Response of a Flexible Pipe with an Incomplete Tensile Armor Layer. *J. Offsh Mech. Arct. Eng.* **2021**, *143*, 051702. [\[CrossRef\]](#)
- Goto, Y.; Okamoto, T.; Araki, M.; Fuku, T. Analytical Study of the Mechanical Strength of Flexible Pipes. *J. Offsh Mech. Arct. Eng.* **1987**, *109*, 249–253. [\[CrossRef\]](#)
- Yim, K.-H.; Jang, B.-S. A Comparative Study for the Prediction of Ultimate Tensile Strength in Flexible Pipes. In Proceedings of the Offshore Technology Conference Asia, Kuala Lumpur, Malaysia, 22–25 March 2016.
- Cornacchia, F.; Liu, T.; Bai, Y.; Fantuzzi, N. Tensile Strength of the Unbonded Flexible Pipes. *Comps. Struct.* **2019**, *218*, 142–151. [\[CrossRef\]](#)
- Xu, Y.; Bai, Y.; Fang, P.; Yuan, S.; Liu, C. Structural Analysis of Fibreglass Reinforced Bonded Flexible Pipe Subjected to Tension. *Ships Offshore Struct.* **2019**, *14*, 777–787. [\[CrossRef\]](#)
- Fang, P.; Xu, Y.; Gao, Y.; Ali, L.; Bai, Y. Mechanical Responses of a Fiberglass Flexible Pipe Subject to Tension & Internal Pressure. *Thin-Walled Struct.* **2022**, *181*, 110107.

29. Zhou, C.; Huang, Z.; Kang, Y.; Zhang, D.; Ye, N.; Sævik, S. The Study of a New Concept of Flexible Pipe with Carbon Fiber/Epoxy Reinforced Inner Sheath. In Proceedings of the ASME 2017 36th International Conference on Ocean, Offshore and Arctic Engineering, Trondheim, Norway, 25–30 June 2017.
30. Liu, Q.; Xue, H.; Tang, W.; Yuan, Y. Theoretical and Numerical Methods to Predict the Behaviour of Unbonded Flexible Riser with Composite Armour Layers Subjected to Axial Tension. *Ocean Eng.* **2020**, *199*, 107038. [[CrossRef](#)]
31. Smith, C.B. Some New Types of Orthotropic Plates Laminated of Orthotropic Material. *J. Appl. Mech.* **1953**, *20*, 286–288. [[CrossRef](#)]
32. Sun, Z.; Huang, W.; Lu, H.; Yan, J.; Yin, Y.; Bu, Y. Study on the Mechanical Characteristics of a Fibre Reinforced Flexible Pipe under Radial Compression Loads. *Front. Mater.* **2023**, *10*, 1118046. [[CrossRef](#)]

**Disclaimer/Publisher's Note:** The statements, opinions and data contained in all publications are solely those of the individual author(s) and contributor(s) and not of MDPI and/or the editor(s). MDPI and/or the editor(s) disclaim responsibility for any injury to people or property resulting from any ideas, methods, instructions or products referred to in the content.